Numerical analysis of WIV phenomenon with two cylinders in series: WIV suppression and energy harvesting

Rongjiang Tang[1,#], Yubin Gu[1,#], Xiaowen Mi[2], Daniil Yurchenko[3], Feng Xu[4], Wanhai Xu[5], Xiaowei Liu[6,*], Junlei Wang[7,**]

[1]School of Mechanical and Electrical Engineering, Guilin University of Electronic Technology, Guilin, 541000, China

[2] Guang xi Zhang Autonomous Region Marine Geological Survey Institute

[3] Institute of Sound and Vibration, University of Southampton, SO17 1BJ, UK

[4] Harbin Institute of Technology (Shenzhen), Shenzhen 518055, China

[5] State Key Laboratory of Hydraulic Engineering Simulation and Safety, Tianjin University, Tianjin, 300072, China

[6] School of Aerospace Engineering, Huazhong University of Science and Technology, Wuhan 430074, China.

[7] School of Mechanical and Power Engineering, Zhengzhou University, Zhengzhou, 450000, China

*Corresponding author: Xiaowei Liu; Email: liuxiaowei@hust.edu.cn

**Corresponding author: Junlei Wang; Email: jlwang@zzu.edu.cn

Abstract

Arranging an elastic bluff body in the wake of a fixed upstream bluff body can cause wake-induced vibration (WIV), which includes various hydrodynamic characteristics. This paper numerically studies a dynamic response of the downstream vibrating cylinder with another cylinder fixed upstream under different spacing ratios (α) and radius ratios (φ) of a series of circular cylinders and a series of square cylinders. The results show that as the spacing ratio increases, the series of square-cylinder system can effectively suppress vibration within the interval of α = 5.3 - 5.7, $6 \leq U_r \leq 8$. Subsequently, the influence of different radius ratios has been studied. It is found that as the radius ratio increases, the vibration of the downstream square cylinder transit from VIV to galloping. Besides, it can be found that the power at φ = 2 is higher than that in the other two cases, and the power when α = 6 is much greater than that of the case α = 8 and 4. Finally, the short-time Fourier transform and wavelet transform have been employed to perform time-frequency analysis of different cases with changing the radius ratio. It is shown that the frequency characteristics of the series square-cylinder system are more complicated than those of the circular-cylinder system.

Keywords: Energy harvesting, wake-induced galloping, vortex-induced vibration, cylinders in tandem, computational modeling

1. Introduction

In recent years, large numbers of papers have been focused on the research of vortex-induced vibration (VIV). VIV [1] is a classic flow-induced vibrations (FIVs) phenomenon produced by the coupling of fluid and bluff body when the fluid flows around the elastic bluff body. After von Kármán discovered the classic vortex street phenomenon, many researchers began to study the mechanism and control methods of VIV. Some of the researchers have carried out corresponding investigations on the structure and shape of the vibrating cylinder, and the upstream and downstream flow around it. Zhu et al. [2] numerically analyzed the FIVs of a trapezoidal cross-section bluff body at different angles of attack (0°,90°, and 180°). During the study, a full interaction between VIV and galloping has also been observed. Wang et al. [3] discussed the application of metasurface in the design of aerodynamic systems. They found that different metasurface patterns can effectively suppress or enhance the VIV of a single cylindrical bluff body.

However, the influence of wake-induced vibration (WIV) has also played an important role. WIV occurs when multiple bluff bodies are arranged in a group, while the downstream bluff body is completely immersed in the wake of the upstream bluff body. At the same time, the bluff body can be excited by the upstream wake vortex and fluid force to vibrate periodically. Researchers have conducted theoretical and experimental investigations on the series two-cylinder system. Bokaoan et al. [4] studied wake-induced galloping (WIG) between two interfering cylinders. It is concluded from the dynamic experimental results that due to the separation and structural damping of the cylinder itself, the cylinder exhibits VIV, galloping, or a combination of VIV and galloping. Moreover, Assi et al. [5] experimentally proved that the rotating parallel plate can effectively suppress wake-induced vibration. To further understand the excitation mechanism of the WIV phenomenon with two cylinders in series, Assi et al. [6] also suggested that the WIV of the downstream cylinder is excited by the unstable vortex-structure interaction between the bluff body and the upstream wake, and if the unstable vortex in the upstream wake is removed, WIV will no longer be excited. Subsequently, Assi et al. [7] introduced the concept of wake stiffness based on the fluid dynamics effect and conducted experimental investigations. The results show that although the unstable vortex-structure interaction provides the energy input to sustain the vibration, the wake stiffness defines the characteristics of the WIV response.

With the in-depth study of the motion mechanism of WIV, researchers have also carried out corresponding explorations on factors such as mass ratio, damping ratio, and multiple degrees of freedom [8-12], which may excite or suppress the vibration of the vibrating cylinder. In addition, many researchers have begun to study the WIV of bluff bodies with different cross-sections. Tamimi et al. [13] numerically studied the WIV of the fixed upstream circular cylinder and the downstream vibrating square cylinder. It is found that compared with two circular cylinders arranged in tandem, the freely mounted downstream square cylinder displays a VIV response, and there is no galloping or wake-induced galloping. Zhang et al. [14] conducted numerical simulations on five groups of bluff bodies with different cross-sectional shapes mounted in tandem in the range of 2 - 50 diameters. They found that when the spacing is less than 5 diameters, the VIV response of the upstream cylinder is suppressed and the VIV response of the square cylinder is lower than that of all other bluff bodies. In contrast, the cylinder is more susceptible to wake effects.

In the research of energy harvesting, Bernitsas et al. [15] for the first time proposed and clearly defined the concept of "Vortex-Induced Vibration for Aquatic Clean Energy" (VIVACE) in 2008. Mehmood et al. [16] connected the piezoelectric transducer to the transverse degree of freedom to implement a VIV piezoelectric energy harvester (VIVPEH) and then performed a comprehensive numerical analysis based on the Reynolds number. It was also found that the load resistance has a greater impact on the oscillation amplitude, lift coefficient, and voltage output. Besides, Latif et al. [17] studied the energy harvesting characteristics of C-shaped cylinders with different cut angles through experiments. To enhance flow-induced motion (FIM) and improve the efficiency of VIVACE, Ding et al. [18] used passive turbulence control (PTC) in the form of roughness strips. It turned out that when $30000 \leq Re \leq 110000$, transition from VIV to galloping can be initially found at

Re = 90000 with a "P + 2S + P + S" (P = pair and S = single) pattern. In addition to numerical simulation and experimental research on multi-cylinder series, Zhang et al. [19] also used deep learning to predict the piezoelectric energy harvesting of wake galloping.

It can be found that the existing research on WIV is mainly focused on vibrations of a circular cylinder, and there are few theoretical studies on the WIV of square cylinders arranged in tandem except some experimental investigations. Therefore, this paper uses numerical simulation to study the WIV of square cylinders arranged in tandem. In addition, more researches are focused on the study of spacing ratio, mass ratio and different Reynolds numbers, and few papers analyze the diameter ratio of the upstream and downstream's cylinders in tandem. In this paper, the upstream bluff body is set as a fixed elastic square cylinder, and the downstream one is set as a single-degree-of-freedom elastic square cylinder that can move in a cross-flow direction. The rest of the paper is divided as follows. In section 2, the governing equation of the system is introduced. To better observe the WIV under different conditions, the reduced velocity is controlled in the range of 2 - 12 and the Reynolds number change interval is 5301 - 31811. The model establishment and FIVs of the series circular-cylinder system are studied in section 3. In section 4, the vibration characteristics of the series square-cylinder system are simulated and analyzed. Table 1 shows the variables and their corresponding symbols used in this paper.

Table 1 Nomenclature.

L	Cylinder length
Re	Reynolds number
U	Mean flow velocity
$U_r = U/(f_n D)$	Reduced velocity
ρ	Water density
$f_n = \sqrt{K/(m+m_a)}/2\pi$	Natural frequency
f	Vibration Frequency
y	Amplitude in Y direction
D	Cylinder diameter
C_l	Lift coefficient
C_d	Drag coefficient
P_0	Mechanical power
K	Spring stiffness
φ	Radius ratio
m	Oscillating system mass
m_a	Added mass

α	Spacing ratio
$m^* = 4m/(\pi\rho D^2 L)$	Mass ratio
C_{total}	System total damping
ζ	Damping ratio
μ	Kinetic viscosity of water

2. Governing equation

2.1. Physical model and fluid model

To simplify the model and improve the computational efficiency, this paper adopts a classic "mass-spring-damper" system to study VIV and WIV as the red arrow in Fig. 1 shows. The movement of the cylinder in the y-direction can be expressed by a second-order linear equation [20]:

$$M\ddot{y}(t) + C_{total}\dot{y}(t) + Ky(t) = F_{fluid,y}(t) \tag{1}$$

where M is the total mass of the system, y represents the cylinder's displacement, K is the spring stiffness. C_{total} means the total damping of the whole system, $F_{fluid,y}$ is the fluid force on the vibrating cylinder.

In the research process of this paper, the fluid is considered to be an incompressible viscous fluid [21]. The flow motion passing around a bluff body can be described by the unsteady two-dimensional Reynolds-averaged Navier–Stokes (2D-RANS) equation:

$$\frac{\partial \overline{u_i}}{\partial x_i} = 0 \tag{2}$$

$$\frac{\partial \rho \overline{u_i}}{\partial t} + \frac{\partial \overline{u_i u_j}}{\partial x_j} = \frac{\partial \overline{p}}{\partial x_i} + \mu \nabla^2 \overline{u_i} - \frac{\partial \rho \overline{u_i' u_j'}}{\partial x_j} \tag{3}$$

where $-\rho\overline{u_i' u_j'}$ represents the Reynolds stress and is defined as:

$$-\rho\overline{u_i' u_j'} = \mu_t\left(\frac{\partial u_i}{\partial x_j} + \frac{\partial u_j}{\partial x_i}\right) - \frac{2}{3}\rho k_t \delta_{ij} \tag{4}$$

In the above equations, t represents time, x_i and x_j denote the coordinates of the Cartesian positions in the i and j directions, respectively, u_i and u_i' are the time averaged value, k_t is the turbulent kinetic energy, δ_{ij} is the Kronecker delta function. Respectively, μ and μ_t represent the dynamic viscosity and the turbulent viscosity, p denotes the pressure. Besides, the two-dimensional RANS equation is solved together with

SST (Shear Stress Transport) $k-\omega$ turbulent model which was firstly proposed by Menter [22].

The mechanical power of the downstream cylinder is defined as [23]:

$$P_o = \frac{1}{T_v}\int_0^{T_v} F_{fluid,y}\dot{y}dt \quad (5)$$

where $2\pi/T_v = 2\pi f_v$.

Then combining equation (1) and equation (5):

$$P_o = \frac{1}{T_v}\int_0^{T_v}(M\ddot{y} + C_{total}\dot{y} + Ky)\dot{y}dt \quad (6)$$

Using the method proposed by Zhang et al. [24], equation (6) can be simplified as:

$$P_o = \frac{1}{T_v}\int_0^{T_v} C_{total}\dot{y}^2 dt \quad (7)$$

2.2. Solution methodology

The numerical simulation is carried out in FLUENT, and the user-defined function (UDF) method is used to calculate the displacement of the downstream vibrating cylinder. UDF used in the paper adopts the fourth-order Runge-Kutta method for calculation. UDF calculates and updates information after each iteration, and then uses the results as the initial conditions for the next cycle. At present, the classical fourth-order Runge-Kutta algorithm to solve the initial value problem of a differential equation is defined as follows:

$$y_{n+1} = y_n + \frac{h}{6}(M_1 + 2M_2 + 2M_3 + M_4) \quad (8)$$

$$M_1 = f(x_n, y_n) \quad (9)$$

$$M_2 = f\left(x_{n+1/2}, y_n + \frac{h}{2}M_1\right) \quad (10)$$

$$M_3 = f\left(x_{n+1/2}, y_n + \frac{h}{2}M_2\right) \quad (11)$$

$$M_4 = f(x_{n+1}, y_n + hM_3) \quad (12)$$

where x_n represents a series of discrete nodes, y_n represents the approximate solution corresponding to x_n.

Since the vibration displacement and velocity of the cylinder at the initial moment are both zero, the initial value problem of the second-order differential equation (1) has the following expressions:

$$\ddot{y} = \frac{f_{fluid,y}(t)}{M} - 2\zeta\omega\dot{y} - \omega^2 y \quad (13)$$

where $y(0) = 0$ and $\dot{y}(0) = 0$, ζ denotes the damping ratio of the cylinder, ω is the angular frequency of the cylinder.

Introducing a new variable Z, $Z = \dot{y}$, equation (13) can be transformed into a first-order differential equation as follows:

$$y(0) = 0 \tag{14}$$

$$\dot{Z} = \frac{f_{fluid,y}(t)}{M} - 2\zeta\omega Z - \omega^2 y, Z(0) = 0 \tag{15}$$

3. Model establishment and analysis of two circular cylinders in tandem

This paper studies the WIV of two cylinders in tandem. Huera-Huarte et al. [25] and Nguyen et al. [26] studied the WIV of two cylinders arranged in tandem under different Reynolds numbers and different spacing ratios through experiments and computational fluid dynamics methods. In this section, a series circular-cylinder system is selected for preliminary analysis to compare with the results of the series square-cylinder system as shown in Fig. 1. The two cylinders are aligned to the centerline and the square cylinders are assigned as the same positions. The upstream cylinder is set as a fixed mounted elastic cylinder, and the downstream cylinder is modeled as a single-degree-of-freedom system. The streamwise distance between the two cylinders is represented by αD. Huera-Huarte et al. [25] chose the interval ratio between 4 - 8 during the experiment, and Lin et al. [27] and Zhang et al. [19] chose to study the interval ratio between 2 - 8. Therefore, after comprehensively considering the numerical calculation efficiency and the validity of the data, this paper chooses to conduct simulations in the interval of $4 \leq \alpha \leq 8$. The orange shaded area is a detailed model diagram of the downstream vibrating cylinder. The left side of the calculation domain is set as the velocity inlet, the right side is set as the pressure outlet, and the upper and lower boundaries are set as the free slip boundary. The main parameters and symbols used in the research process of this paper are shown in Table 2.

3.1. Computational grid

As shown in Fig. 2, this paper uses overset grid [28] method for grid division. Overset grids are mainly divided into foreground grid and background grid. Grid areas that are independent of each other overlap in space but do not have a connected relationship. The foreground grid and the background grid are grafted through the "overset" module in FLUENT, where the background grid is generated to discretize the entire flow domain [29], and the body-fitted grid that handles the movement of the cylinder is generated on the foreground grid. Since the overset grid highly depends on interpolation accuracy, a double-precision solver is selected in the calculation process to reduce the calculation error. The working process of overset grids is mainly divided into digging holes, establishing regional connectivity and interpolation calculation. The digging is mainly based on the Cartesian grid method, which uses an unstructured Cartesian grid to surround the grid surface or grid line from the outside, thereby indirectly judging the relationship between internal and external. The establishment of regional connectivity is divided into three steps: 1) Locating boundary points. 2) Identify potential overset grids and search for donor cells. 3) Interpolation calculation is carried out by the boundary exchange method (BEM) and the area exchange method (REM).

3.2. Irrelevance verification

To further verify the calculation accuracy of the model in this paper, this section selects a series of two-circular-cylinder systems with $\alpha = 4$ and $U_r = 5$ as the benchmark for analysis. In the verification of grid independence, three grids G1, G2, and G3 with different densities are selected for comparison and the results are shown in Table 3. It can be found that as the grid density increases, the rate of change of the data becomes smaller, so this paper selects the grid density of G2 as the standard for subsequent research on grid division. Three timesteps of 0.001s, 0.003s, and 0.005s are selected for simulation analysis, and the results are shown in Fig. 3. It can be found from Fig. 3(a) that the differences between the three curves are relatively small. For further study, the Fourier transform is performed on the three different timestep displacements, and the results are shown in Fig. 3(b). It is found that the maximum amplitudes of the three schemes are all obtained around 2.53 Hz, so the calculation consistency of the three timesteps is better. To choose a relatively large timestep to improve the calculation efficiency without affecting the calculation accuracy, this study chooses 0.005s as the standard time step for subsequent research.

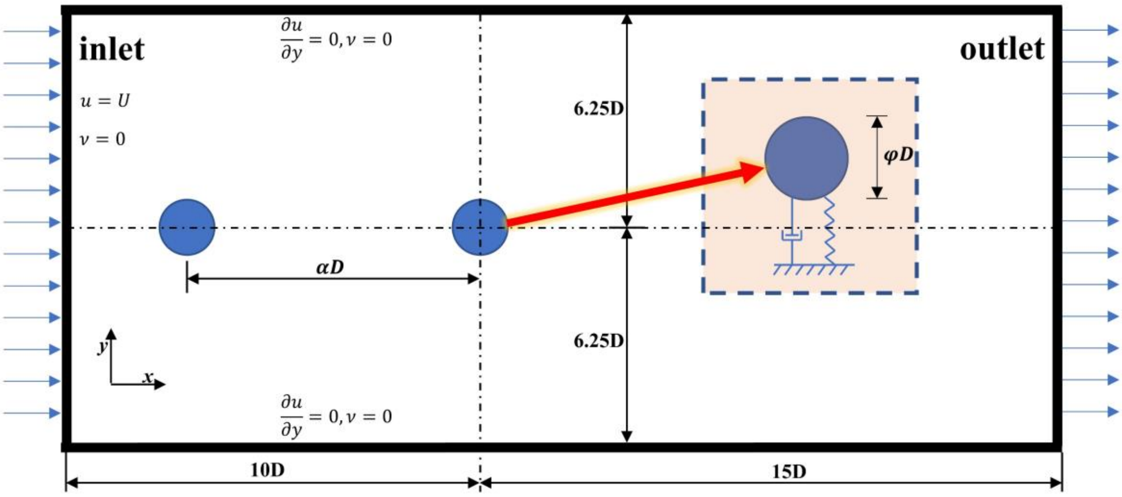

Fig. 1. Physical model diagram of circular cylinders in tandem (circular can be replaced by square).

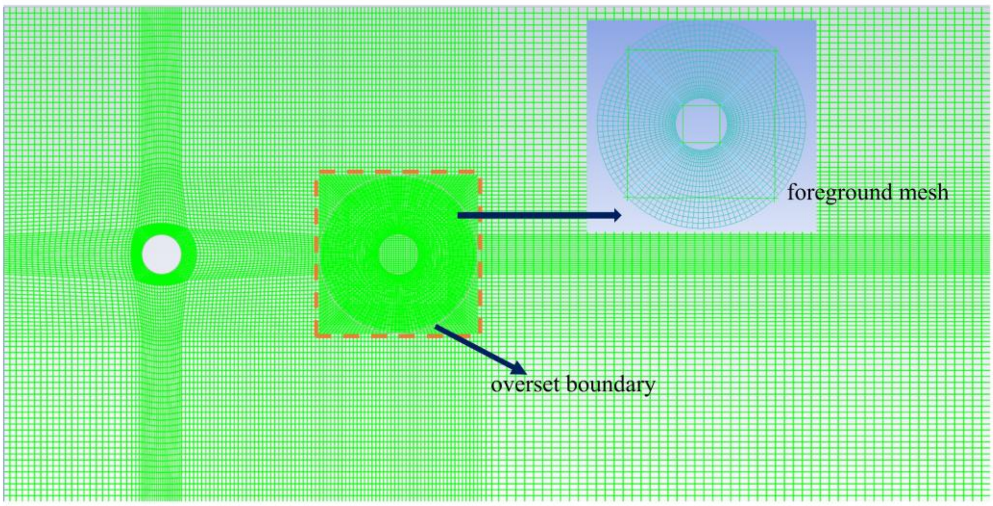

Fig. 2. Computational mesh of the background grid and foreground grid.

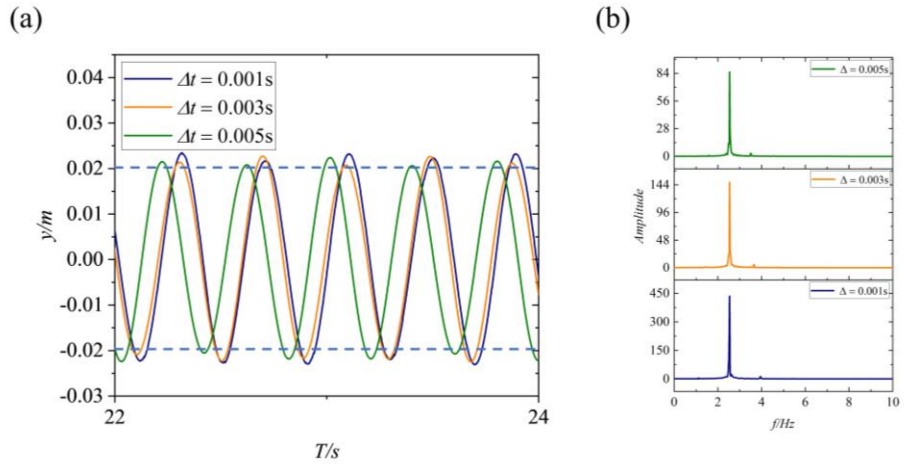

Fig. 3. Independence analysis of three different timesteps.

Table 2 Physical model parameters.

Item	Value
Damping ratio (ζ)	0.001
Diameter of circular and each side of the square cylinder (D)	0.032 [m]
Mass ratio (m^*)	8
Nature frequency (f_n)	2.601 [Hz]
Water density (ρ)	998.2 [kg/m^3]
Kinetic viscosity of water (μ)	0.001003

Table 3. Grid independence review at α = 4， U_r = 5

Grid	Nodes	A.rms		Clrms		Cd.rms	
G1	16124	0.0147	—	0.6801	—	0.77917	—
G2	27298	0.0133	9.52%	0.5501	19.11%	0.78204	0.37%
G3	43717	0.0128	3.75%	0.6140	11.61%	0.72716	7.02%

3.3. Analysis of two-cylinder system arranged in tandem

3.3.1. radius ratio (φ) = 1

The radius ratio φ refers to the ratio of the radius of the upstream cylinder to the radius of the downstream radius. After the relevant parameters are determined, this paper conducts a simulation analysis on the WIV of the two-cylinder system of equal radius (φ = 1) arranged in series or one behind another. During the research process, the change interval of the reduced velocity is selected to be 2 - 12 [21]. Before the analysis, both the single circular cylinder and the single square cylinder are simulated as shown in Fig. 4. The present results are in good consistency with the results reported in Zhu et al. [30] and Tammi et al. [13]. Then simulations of different spacing ratio coefficient α are performed and the results are shown in Fig. 5. It can be found from Fig. 5(b) that no matter how the spacing ratio coefficient α changes, the downstream cylinder always demonstrates VIV. When $2 \leq U_r \leq 4$, VIV is in the initial branch which is marked in blue. Meanwhile, the dimensionless amplitude increases obviously as the reduced velocity increases. Correspondingly, in the figure of dimensionless frequency shown in Fig. 5(a), the frequency curve shows an upward trend when $2 \leq U_r \leq 4$. Then VIV enters the upper branch which is marked in gray when $4 \leq U_r \leq 8$. At this period, the dimensionless frequency of the downstream cylinder is locked in the vicinity of $f_v / f_n = 1$, so this period is also called lock-in. It is worth noting that when $\alpha = 4$, 5, and 6, VIV starts to enter the lower branch when $U_r = 7$, while the remaining groups enter the lower branch which is marked in purple when $U_r = 8$. To sum up, with the increase of the spacing ratio coefficient α, the lock-in interval of the downstream cylinder is increased, and the dimensionless displacement of the cylinder is larger when $\alpha = 5.5$. In general, there is still a difference between the dimensionless frequency of the downstream vibrating cylinder and the VIV of a smooth single cylinder. Interestingly, the dimensionless frequency is locked near unity when $4 \leq U_r \leq 12$, $\alpha = 6.5$ and 8. However, in the classic VIV, the dimensionless frequency always increases with the increase of the reduced velocity. Therefore, the case of $\alpha = 6.5$ and 8 can effectively control the vibration frequency without increasing or decreasing. In addition, except for $\alpha = 5.5$, the dimensionless frequencies of several other cases tend to drop suddenly to zero, which also shows that when $\alpha = 4$, 5, and 6, including the largely reduced velocity, the series circular-cylinder system can suppress vibration. Fig. 6 shows the variation of the root mean square value of the lift coefficient under different spacing ratio coefficients α. The lift coefficient curves of different spacing ratios except $\alpha = 8$ all show an upward trend when $2 \leq U_r \leq 4$, in the case of $\alpha = 8$, the lift coefficient curve just rises to $U_r = 3$ and then enters the descending range. It can be found from Fig. 6 that the lift coefficient curve is steeper at α = 8 than in other cases when $2 \le U_r \le 3$, which corresponds to the same segment in the dimensionless amplitude in Fig. 5(b). In general, the value of the lift coefficient curve of α = 8 is lower than that of the other cases, which is reflected in the dimensionless amplitude change diagram as a lower amplitude in the lock-in region.

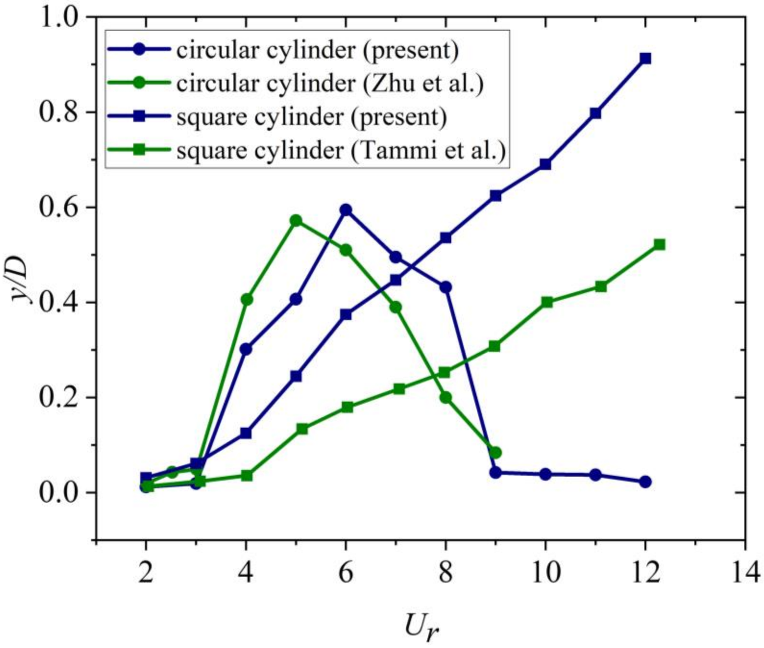

Fig. 4. Validation of the numerical model of a single circular/square cylinder.

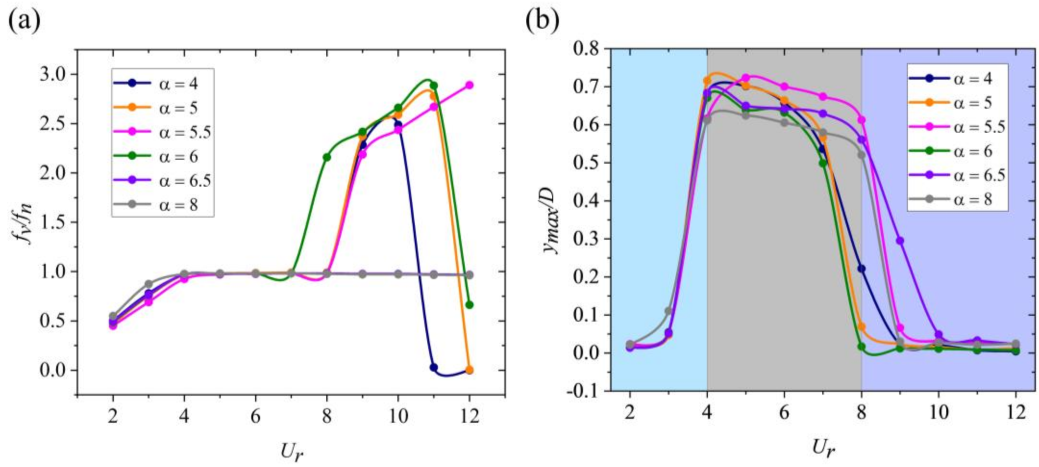

Fig. 5. The vibration characteristics of the downstream circular cylinder: (a) diagrammatic of dimensionless frequency and (b) diagrammatic of dimensionless displacement.

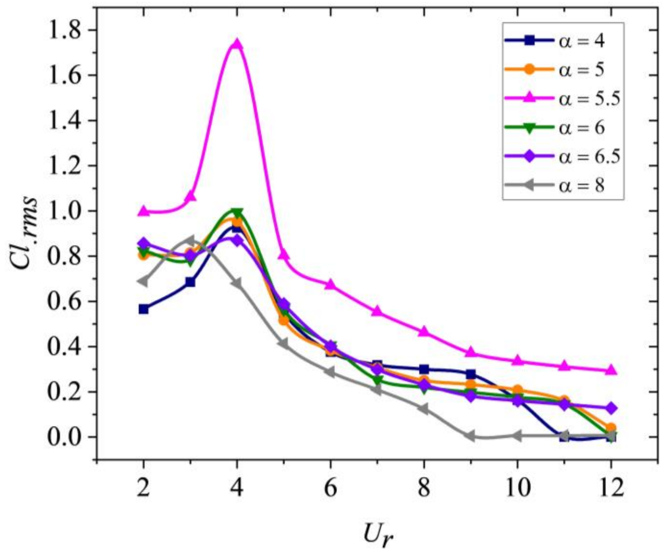

Fig. 6. Comparison curve of root mean square change of lift coefficient of the downstream circular cylinder at different spacing ratio coefficients (α).

3.3.2. Comparison of different radius ratios

Having completed the analysis of the series circular-cylinder system with φ = 1, consider the cases of spacing ratio α = 6, φ = 2, and φ=3 respectively to determine the influence of the change of the radius ratio on the WIV of the series circular-cylinder system in series. It can be seen from Fig. 7(a) that when the radius ratio φ = 1, the dimensionless amplitude curve of the downstream vibrating cylinder shows a clear VIV. When φ = 2, the vibration of the downstream cylinder still reflects the characteristics of VIV, but the lock-in interval is not observed. Interestingly, when φ = 3, the dimensionless amplitude curve of the downstream vibrating cylinder shows obvious fluctuations, and it is impossible to confirm whether it is VIV or galloping in this case. Correspondingly, in Fig. 7(b), the dimensionless frequency of φ = 3 increases first and then decreases in the interval of $2 \leq U_r \leq 5$. Since then, the frequency has been on an upward trend. The irregular vibration of the downstream cylinder is caused by the presence of multiple frequencies. The specific content is explained below through short-time Fourier transform and wavelet transform.

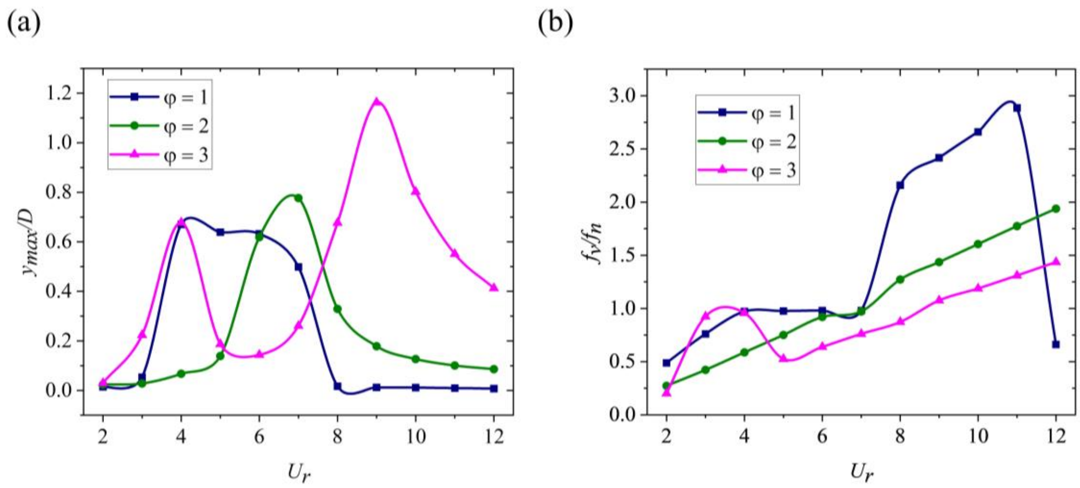

Fig. 7. Comparison of the vibration characteristics of the downstream circular cylinder with different radius ratios (φ): (a) diagrammatic of dimensionless displacement and (b) diagrammatic of dimensionless frequency.

4. Analysis of two-square-cylinder system arranged in tandem

4.1. radius ratio (φ) = 1

Fig. 8 is a diagram showing the vibration characteristics of the series square-cylinder system with different spacing ratio coefficients. It can be seen from Fig. 8(a) that when $2 \leq U_r \leq 6$, the dimensionless displacements of different spacing ratio cases all increase with the increase of the reduced velocity in the light blue area on the left side of the diagram. It can be seen from the purple area in the diagram ($8 \leq U_r \leq 12$) that the dimensionless displacements of different spacing ratio cases also decrease with the increase of the reduced velocity. Note, that $6 \leq U_r \leq 8$ is a relatively special interval, which is marked in gray in the diagram, where the changes in the amplitude of α = 5, 6, and 6.5 first increase and then decrease (rising to the maximum amplitude and then decreasing), but when α = 4, 5.5 and 8, the dimensionless displacement curve appears to decrease first and then increase. Among them, α = 4 and 8 only slightly decrease and then increase. It is interesting that the case α = 5.5 exhibits a sudden drop. Fig. 8(b) is diagrammatic of corresponding dimensionless frequency. It can be seen intuitively that as the reduced velocity increases, the dimensionless frequency of each case also increases, however, the reduced velocity fluctuates in the range of 6 - 8. For further observation, the dimensionless frequency curve of $6 \leq U_r \leq 8$ is enlarged in the red block diagram of Fig. 8(b). It can be found that when $\alpha = 4$, the dimensionless frequency is locked in the vicinity of unity, and the dimensionless frequency curve of $\alpha = 8$ shows obvious fluctuations. In general, the dimensionless displacement is larger than others when $\alpha = 6.5$, and the change of the dimensionless frequency is relatively stable.

To analyze the specific force of the square cylinders in series, this paper also calculates the root mean square value of the lift coefficient and the mean value of the drag coefficient, as shown in Fig. 9. It can be seen from Fig. 9(a) that the lift coefficient values of different spacing ratios oscillate and fluctuate between 0 - 2.3, and when $5 \leq U_r \leq 8$, the lift coefficients of several cases all appear to drop first and then rise. The red box is a partially enlarged view of $8 \leq U_r \leq 9$. It can be found that when $\alpha = 4 - 6.5$, the lift coefficient is in an increasing trend, and when $\alpha = 8$, the lift coefficient is locked at 1.25. Fig. 9(b) shows the change of the mean value of the drag coefficient. From the diagram, it can be found that the change of the mean value of the drag coefficient is similar to the curve of the root mean square value of the lift coefficient. In general, the value of the curve of $\alpha = 6.5$ is larger than that of the other several cases. Compared with Fig. 6, the lift coefficients of the square cylinder and the circular cylinder show a great difference. The lift coefficient curve of the circular cylinder enters a downward trend after a small rise. While the lift coefficient curve of the square cylinder shows a " V " shape between $4 \leq U_r \leq 9$, which may be a special property caused by different cross-sectional shapes.

In order to verify the particularity of the gray interval ($6 \leq U_r \leq 8$) shown in Fig. 8(a), this paper carried out another analysis: the spacing ratio is selected from 5.3 to 5.7, and the results are shown in Fig. 10. It can be found in Fig. 10(a) that when $6 \leq U_r \leq 8$, the dimensionless amplitudes of the five different spacing ratio cases all appear a sudden drop. Among them, when $\alpha = 5.5$, 5.6, and 5.7, the lowest points are all near zero. It is worth noting that when $\alpha = 5.6$, the sudden drop interval is advanced, and when $\alpha = 5.7$, the sudden drop interval lags. The dimensionless frequency shown in Fig. 10(b) increases with the increase of the reduced velocity. There is no sudden drop or lock-in region. Therefore, the series square-cylinder system can exhibit obvious vibration suppression in the interval of $5 \leq U_r \leq 8$.

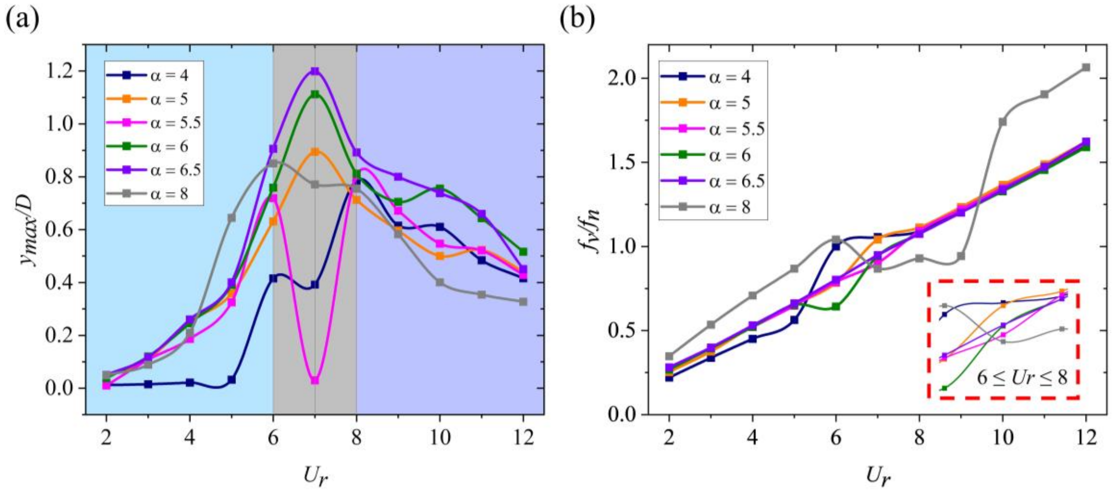

Fig. 8. Comparison of the vibration characteristics of the downstream square cylinder with different spacing ratios (α): (a) diagrammatic of dimensionless displacement and (b) diagrammatic of dimensionless frequency.

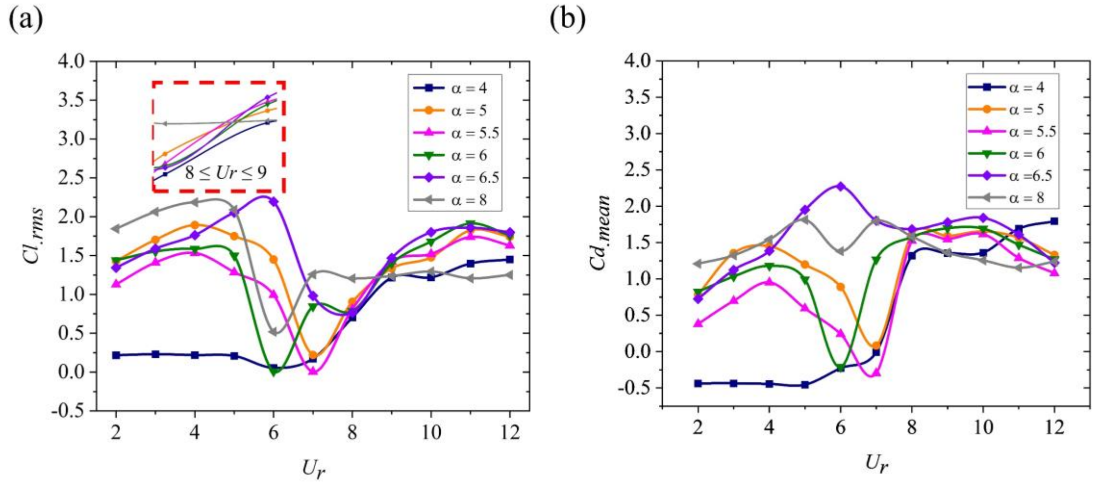

Fig. 9. (a) Comparison of root mean square change of the lift coefficient of different spacing ratio coefficients (α); (b) Comparison of the mean value of the drag coefficient of different spacing ratio coefficients (α).

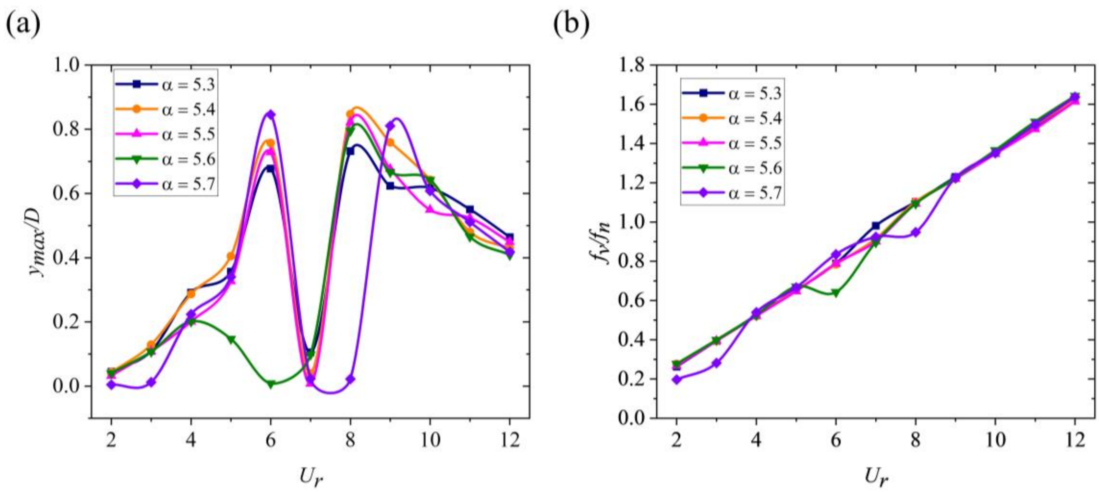

Fig. 10. Detailed analysis of the vibration characteristics of the downstream square cylinder when $5.3 \leq \alpha \leq 5.7$: (a) diagrammatic of dimensionless displacement and (b) diagrammatic of dimensionless frequency.

4.2. Comparison of different radius ratios of the square-circular system

Fig. 11 shows the comparison of the vibration characteristics of different spacing ratios α = 4, 6, and 8 in the three cases of radius ratios φ=1,2 and 3, respectively. It can be found that when φ = 1, the dimensionless amplitudes of the three spacing ratio cases all reflect the characteristics of VIV, and when $6 \leq U_r \leq 8$, the dimensionless frequency is also locked in the vicinity of unity. It is worth noting that when φ = 2, the dimensionless amplitudes of the three spacing ratio cases show obvious galloping. Meanwhile, the dimensionless displacement of the downstream cylinder increases with the increase of the reduced velocity. When φ = 3, the downstream cylinder still shows galloping, and the galloping is more obvious. When α = 4 and 8, the dimensionless amplitude of the downstream cylinder in the interval of $2 \leq U_r \leq 9$ is very small and closes to zero at φ = 2, then the dimensionless amplitudes of the two cases start to increase when $9 \leq U_r \leq 12$, and the corresponding dimensionless frequency is also in an increasing trend. By comparison, the downstream cylinder at φ = 2 does not have the same amplitude as the other two cases (α = 4 and 8) when α = 6, its dimensionless amplitude becomes larger as the reduced velocity increases. In Fig. 11(b), it can be found that the dimensionless frequency increases as the reduced velocity increases, except for two cases (α = 8, φ = 1 and 2). These two cases show a V-shape trend of their dimensionless frequency lines when $6 \leq U_r \leq 10$. In general, as the radius ratio increases, the series square cylinders exhibit completely different characteristics than the series circular cylinders. The vibration characteristics of the downstream vibrating cylinder gradually transition from VIV to galloping. When it comes to the mechanisms of VIV and galloping, Bernitsas et al. [31] found that two mechanisms contribute to VIV: a hydrodynamic excitation and a mechanical restoring force. In galloping, the driving mechanism is instability in a steady direction. This interesting phenomenon was also observed by Ding et al. [18], which was introduced in the introduction part.

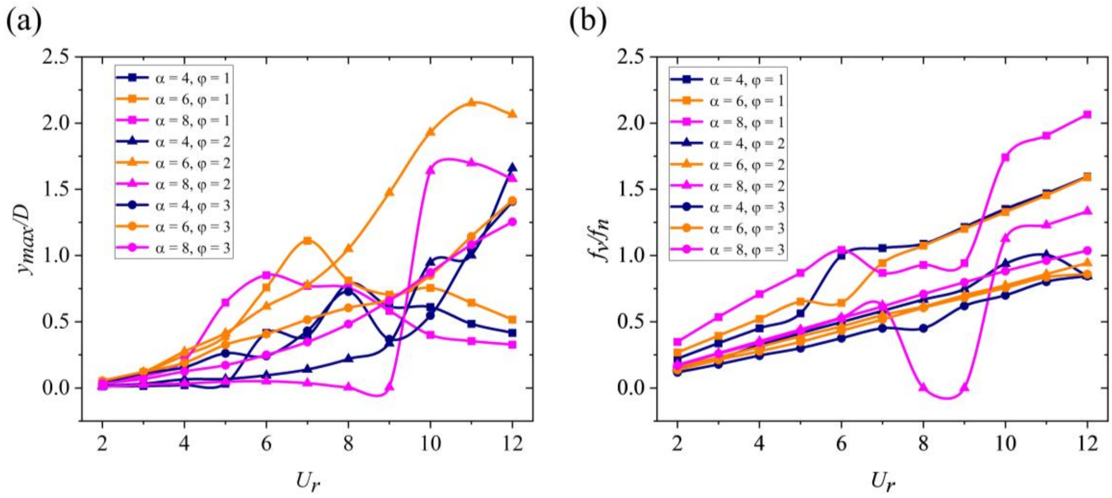

Fig. 11. Comparison of the vibration characteristics of the downstream square cylinder with different spacing ratios and radius ratios: (a) diagrammatic of dimensionless displacement and (b) diagrammatic of dimensionless frequency.

4.3. Time-frequency analysis of vibration signals

To better compare with the series cylinder system, this paper analyzes several groups of cases with α = 6, φ = 1,2, and 3, as shown in Fig. 12. The data in Fig. 12 has been analyzed above, and here is only used for comprehensive comparison, so its characteristics of dimensionless amplitude will not be repeated. It is more obvious from Fig. 12 that the vibration characteristics of the square-cylinder cases with radius ratios of 2 and 3 are different from other cases. Then several special reduced velocities (U_r = 4, 6, and 9) are taken for local analysis. Because the lift coefficient curve is not always a stable process during the WIV research process, short-time Fourier transform and the complex Morlet wavelet transform [32, 33] are performed on the lift coefficient curve to study the time-frequency characteristics of wake vortices under different conditions. This paper uses the same generating function as Chen et al. [34] to analyze the WIV of the downstream vibrating cylinder. According to the frequency peak value calculated using the fast Fourier transform, a discrete scale set is selected linearly. In the time domain the complex Morlet wavelet [35] is expressed as：

$$\psi(t) = \pi^{-1/4}\left(e^{i\omega_0 t} - e^{-\omega^2/2}\right)e^{-t^2/2} \tag{16}$$

4.3.1. Circular cylinders arranged in tandem

The results of the circular-cylinder system are shown in Figs. 13 - 15 respectively. Fig. 13(a) and (b) analyze the lift coefficient of the cylinder with φ = 1 and U_r = 4. The FFT transform may generate more interference signals because the signal of the lift coefficient is irregular. Therefore, time-domain analysis of the lift coefficient is carried out to better understand the vibration of the downstream cylinder. It can be found from Fig. 13(a) that the time-frequency concentration is stronger at 5 - 10s, then gradually begins to diverge after 10s and mainly concentrates on low frequencies. In the wavelet analysis shown in Fig. 13(b), it is shown that the frequency components are mainly concentrated in the low frequency of 0 - 0.2Hz, and the high-energy signals are also concentrated in 5 - 10s, which matches the results of the short-time Fourier. This also explains that the vortex shedding is faster at the beginning of the vibration, and the vortex shedding speed gradually decreases with the increase of time. Fig. 13(c) and (d) analyze the lift coefficient of the cylinder with φ = 1 and U_r = 6. It can be seen from Fig. 13(c) that the time-frequency concentration is stronger around 2.5 - 6.5s, and in addition to the 0 - 8Hz region, the frequency concentration is divergent in the 8 - 13Hz region. In the Morlet wavelet transform, it turns out that in addition to the concentration of high energy bands at 0.3Hz near 5s, there is also a short energy frequency band concentrated in 15 - 50s with an interval of 10s between the frequency components of 0.4 - 0.5 Hz. Similarly, the lift coefficient of the cylinder with φ = 1 and U_r = 9 is analyzed. It can be seen from the short-time Fourier transform curve that the time-frequency concentration between 2 - 10Hz is very strong, and there is no obvious divergence. In contrast, it can be further found in Fig. 13(f) that the energy is relatively strong in the frequency component between 0.4 - 0.5 Hz and concentrated in the vicinity of

5s, and there is no interference of other frequencies. Combining the three situations, it can be found that as the reduced velocity increases, the frequency components of the system are gradually increasing.

Fig. 14(a) and (b) analyze the lift coefficient of the cylinder with $\varphi = 2$ and $U_r = 4$. It can be seen from the short-time Fourier diagram Fig. 14(a) that the time-frequency intensity is concentrated at 0 - 5Hz, and a small divergence phenomenon occurs at about 8.5s. For further analysis, wavelet transform is performed on the lift coefficient. It can be found that there are low-frequency components between 0 - 0.35Hz, and the frequency components between 0.1 - 0.5Hz and 47 - 50s have stronger frequency energy. It is interesting that in the same period, the frequency component has a crescendo trend in the range of 0 - 0.1Hz. Fig. 14(c) and (d) analyze the lift coefficient of the cylinder with $\varphi = 2$ and $U_r = 6$. It can be seen from the short-time Fourier diagram that there is an obvious divergence at 10 - 15Hz. To judge whether there is a disorder in the lift coefficient in this state, it can be found from Fig. 14(d) that there are obvious frequency components between 0.1 and 0.2 Hz, and they are concentrated in 1 - 7s. In addition, there are weaker frequency components at 0.5 - 0.6 Hz and 0.9 - 1 Hz. Fig. 14(e) and (f) analyze the case of $\varphi = 2$ and $U_r = 9$. Meanwhile, the time-frequency intensity stratification of the short-time Fourier diagram is more obvious, gradually decreasing and diverging from 0-8Hz, 8-15Hz to 15-21Hz. In the real part graph of the wavelet transform, it can be observed that there are four frequency components between 0.2 - 0.29Hz, 0.29 - 0.35Hz, 0.5 - 0.6Hz, 0.8 - 0.9Hz, respectively. Among them, the frequency components appearing at 0.29-0.35Hz have greater energy between 47-50s. In general, under the condition of $\varphi = 2$, the time-frequency intensity of the lift coefficient has obvious divergence, indicating that the wake vortex of the front fixed cylinder has already affected the rear vibrating cylinder at this time, which is no longer an ordinary VIV.

Fig. 15(a) and (b) analyze the lift coefficient of the cylinder with $\varphi = 3$ and $U_r = 4$. From the diagrammatic of the short-time Fourier transform, it can be found that the time-frequency intensity gradually diverges from 5s, and the frequency intensity spreads from 0 Hz to 15 Hz. It is worth noting that when the frequency component is 0 - 0.1Hz, the high-energy frequency in the Morlet real part variation graph is concentrated in 6.5 - 17.5s and 46 - 50s. This is quite different from the previous case of φ = 1 and 2, where the high-energy frequency band generally only appears at the beginning of the end. Fig. 15(c) and (d) analyze the lift coefficient of the cylinder with φ = 3 and U_r = 6. In the short-time Fourier transform graph, it turns out that the time-frequency concentration remains strong in 10 - 50s, and it is mainly concentrated in 0 - 5Hz, followed by 5 - 10Hz. Compared with the time-frequency concentration divergence phenomenon in other situations, the phenomenon of strong divergence appears at this time. While in the Morlet wavelet transform graph, there is an obvious frequency component band between 0.35 - 0.42Hz, and it is mainly concentrated in 18 - 48s, which shows that the movement of the vibrating cylinder is strong in the period of 18 - 48s. Fig. 15(e) and (f) analyze the lift coefficient of the cylinder with φ = 3 and U_r = 9. At this period, the short-time Fourier transform diagram has obvious stratified divergence like φ = 2 and U_r = 9. The time-frequency intensity is not only concentrated in the 0 - 6Hz region but also diverges to the 6 - 22Hz region, and as time increases, the frequency signal also shifts to higher frequencies. In the real part change graph obtained by Morlet wavelet transform, the frequency of occurrence can be further refined and analyzed. It can be found that there are obvious bands at 0.2 - 0.3 Hz and 0.6 - 0.7 Hz, indicating that the VIV at this time has two obvious frequency components. This also explains the existence of two peaks in the dimensionless displacement curve of φ = 3 in Fig. 7(a). The frequency component of 0.2 - 0.3Hz has the maximum energy at 18 - 22s. Correspondingly, the frequency component of 0.4 - 0.7Hz has the maximum energy at 47 - 50s.

In the comparative analysis of series circular-cylinder systems with different radius ratios at three different reduced velocities, it can be found that when U_r = 4 and 6, the time-frequency concentration of different radius ratios is almost in the range of 0 - 5 Hz, and the frequency components are also mainly concentrated in the 0.1 - 0.3Hz interval. However, when U_r = 9, the frequency concentration will transition to high-frequency stratification, and there are two frequency bands at φ = 2, U_r = 9 and φ = 3, U_r = 9. In this case, WIV has a dual-frequency effect.

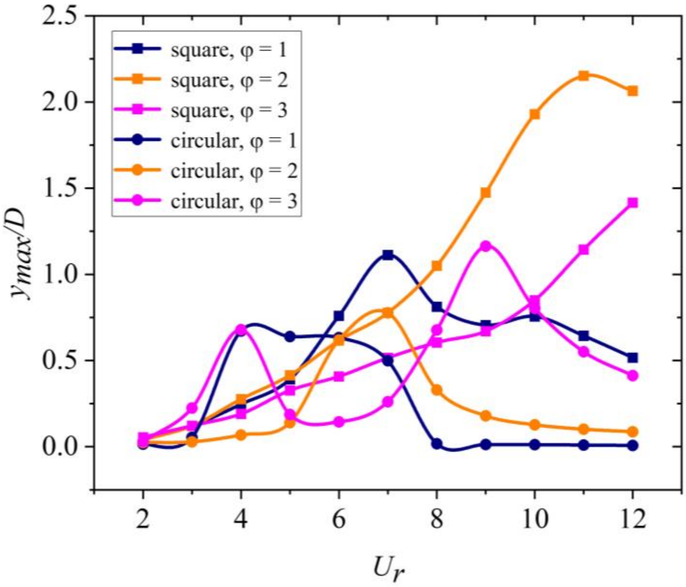

Fig. 12. Dimensionless amplitude changing diagram of the square-cylinder system and circular-cylinder system when the radius ratio φ = 1, 2, and 3.

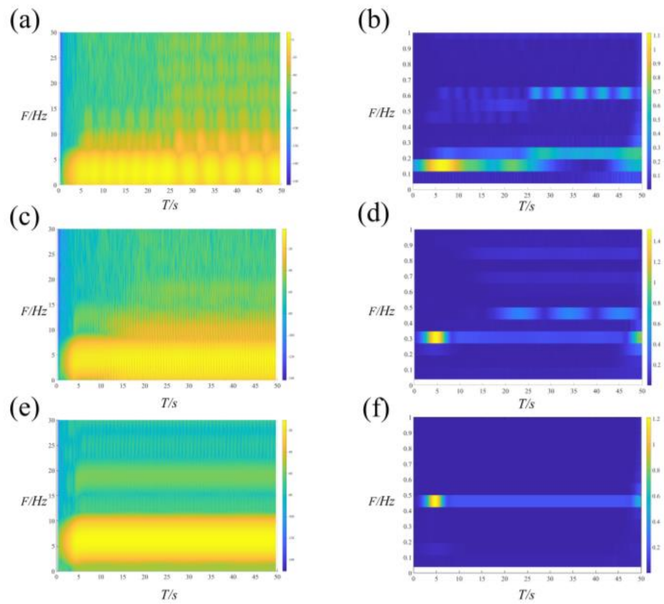

Fig. 13. (a), (c) and (e) are diagrams of Short-time Fourier transform, (b), (d), and (f) are diagrams of Complex Morlet wavelet transform.

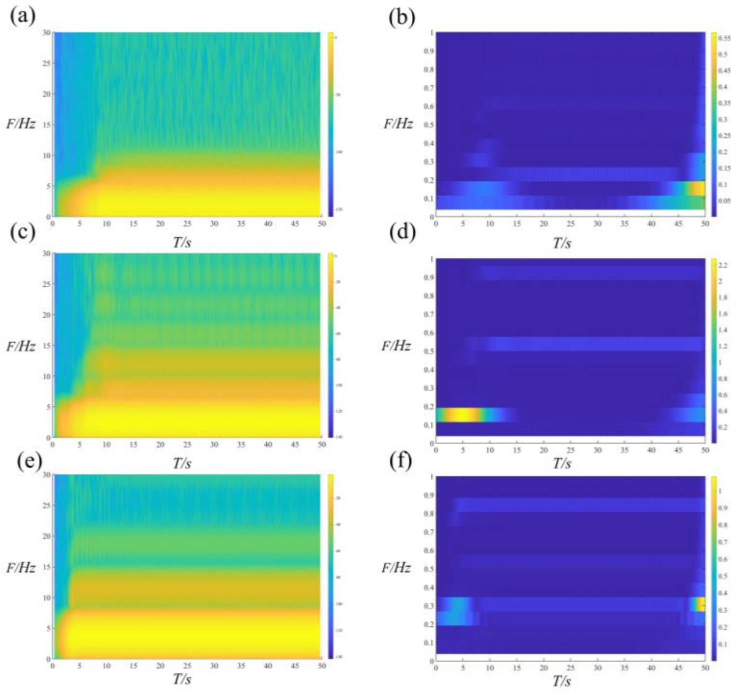

Fig. 14. (a), (c) and (e) are diagrams of Short-time Fourier transform, (b), (d), and (f) are diagrams of Complex Morlet wavelet transform.

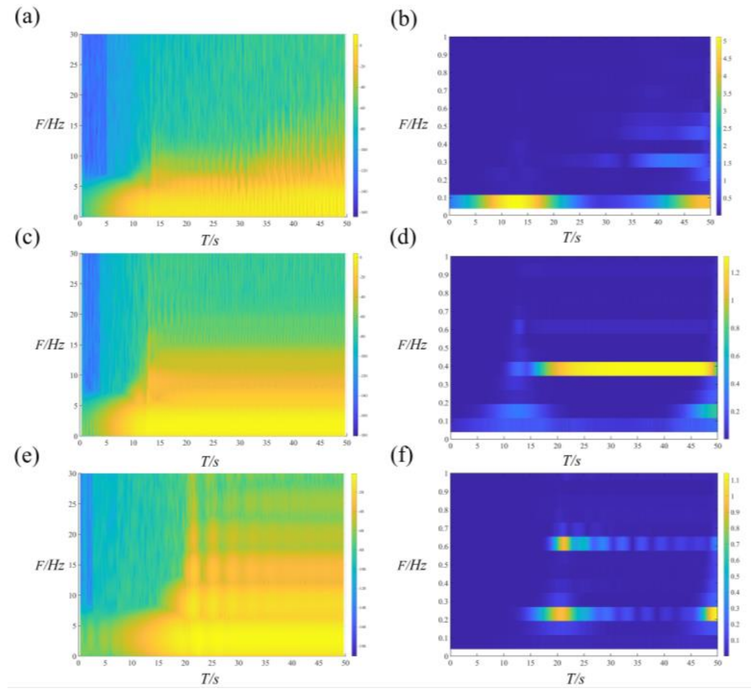

Fig. 15. (a), (c) and (e) are diagrams of Short-time Fourier transform, (b), (d), and (f) are diagrams of Complex Morlet wavelet transform.

4.3.2. Square cylinders arranged in tandem

The results of the square-cylinder system are shown in Figs. 16 - 18 respectively. Fig. 16(a) and (b) analyze the lift coefficient of the cylinder with φ = 1 and U_r = 4. It can be seen from Fig. 16(a) that the time-frequency concentration is stronger in 25 - 50s, and concentrated in the low-frequency range of 0 - 5Hz. In the Morlet wavelet transform graph, two frequency components can also be observed at 20 - 50s, and the energy in the frequency band of 0.1 - 0.2Hz is stronger at 27 - 35s. Fig. 16(c) and (d) analyze the lift coefficient of the cylinder with $\varphi = 1$ and $U_r = 6$. Interestingly, the time-frequency intensity displayed in the short-time Fourier diagram at this time has a periodic jump, while only one frequency component at 0.1 - 0.2Hz can be observed in the Morlet wavelet transform diagram. Different from the previous two cases, when $\varphi = 1$ and $U_r = 9$, the time-frequency signal concentration in Fig. 16(e) has obvious divergence. In the wavelet transform graph, there are three frequency components, and the frequency component at 0.2 - 0.3Hz has the highest energy.

Fig. 17(a) - (f) analyzes the lift coefficient of the cylinder with $\varphi = 2$ and $U_r = 4$. It can be found that the short-time Fourier time-frequency concentration at the three reduced velocities all have different degrees of divergence starting from 15s. This is due to the fluid force on the downstream cylinder and the upstream fixed cylinder after the radius is increased. The balance of the forces of the wake vortex is broken. At this period, the frequency components in Fig. 14(b), (d), and (f) are relatively large, but at least three obvious frequency components appear. When $U_r = 4$, the main frequency components appear at 0 - 0.1Hz and the energy produced in 15 - 33s is higher. When $U_r = 6$, the main frequency component appears in 0.1 - 0.2Hz and the energy is higher in 38 - 45s. When $U_r = 9$, the main frequency component appears at 0.1 - 0.2Hz and the energy is higher within 5 - 12s.

Fig. 18(a) - (f) analyzes the lift coefficient of the cylinder with $\varphi = 3$ and $U_r = 4$. Because the lift coefficient curve is irregular, the time domain analysis of the lift coefficient is carried out, so that its time-domain characteristics can be better judged. Compared with Fig. 17, the dispersion degree of time-frequency concentration at $\varphi = 3$ is much reduced, but there is still divergence at 5 - 15Hz. Moreover, the frequency components in the wavelet transform graph are also reduced compared to $\varphi = 2$, but there are still more than three obvious frequency components. When $U_r = 4$, the main frequency component appears at 0

- 0.1Hz and the energy output is higher at 35 - 45s. The main frequency component appears at 0.1 - 0.2Hz and the energy is higher in the two time periods of 30 - 35s and 37 - 50s when U_r = 6. Besides, the main frequency component appears in 0.1 - 0.2Hz and the energy is higher in 3 - 8s when U_r = 9.

In summary, it can be found that the frequency characteristic of the series square-cylinder system is more complicated than the frequency characteristic of the series circular-cylinder system, and there are more frequency components. This may also be the reason why galloping may occur in the square-cylinder system when the radius is increased, while the circular-cylinder system only displays the VIV or irregular VIV. Short-time Fourier and Morlet wavelet transform can only perform time-frequency analysis on vibration frequencies, but cannot analyze the state of wake vortex.

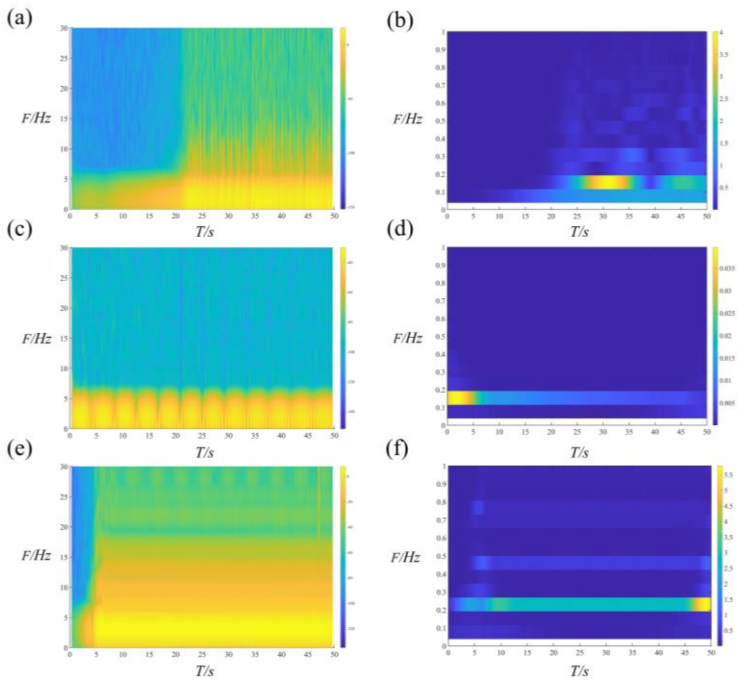

Fig. 16. (a), (c) and (e) are diagrams of Short-time Fourier transform, (b), (d), and (f) are diagrams of Complex Morlet wavelet transform.

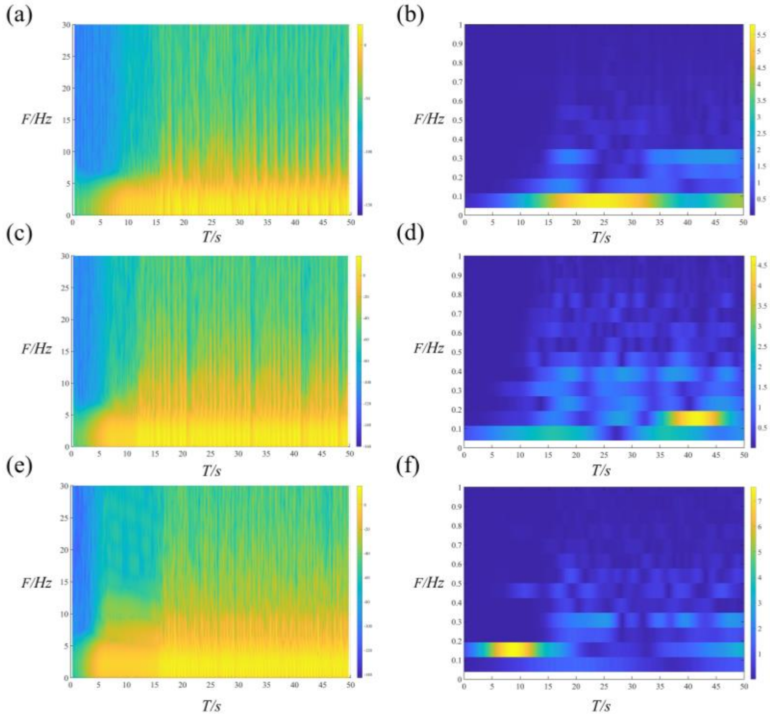

Fig. 17. (a), (c) and (e) are diagrams of Short-time Fourier transform, (b), (d), and (f) are diagrams of Complex Morlet wavelet transform.

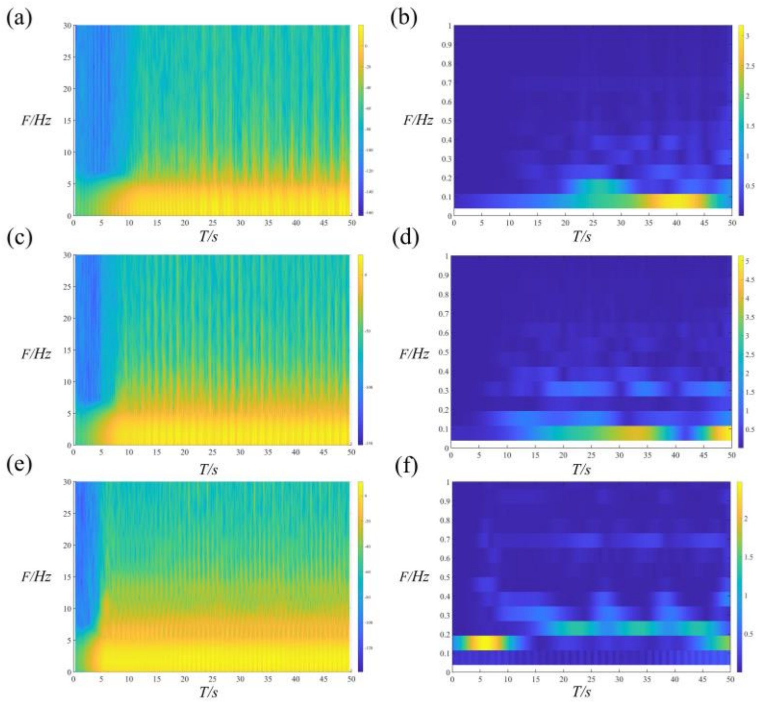

Fig. 18. (a), (c) and (e) are diagrams of Short-time Fourier transform, (b), (d), and (f) are diagrams of Complex Morlet wavelet transform.

4.4. Energy harvesting

Bernitsas et al. [15] proposed and clearly defined Vortex-Induced Vibration Aquatic Clean Energy (VIVACE) when studying flow-induced vibrations. Wang et al. [36] and Zhang et al. [19] also expanded their research on wake galloping piezoelectric energy harvesters (WGPEHs) in subsequent studies. The transition of VIV-galloping discovered by changing the radius ratio and spacing ratio of series square cylinders in this paper can also be a good supplement to theoretical research in this field

After analyzing the characteristics of the downstream cylinder, the power change graph of the model is obtained through calculation as shown in Fig. 19. It can be found that the power at φ = 2 is larger than the other two cases, the power of the case α = 6 is much greater than that of the case α = 8, and the energy harvesting power of the case α = 4 is smaller but relatively larger than φ = 1 and 3. The red block diagram is a partial enlargement of $7 \leq U_r \leq 12$. It can be found that the power of each case is not much different in the stage of $2 \leq U_r \leq 8$. Starting from $U_r \geq 8$, the downstream cylinder begins to appear galloping as the radius ratio increases. Meanwhile, the amplitude becomes significantly larger with the increase of the reduced velocity, so the energy harvesting power also increased. This is of great significance to the research of wake galloping piezoelectric energy harvesters (WGPEHs).

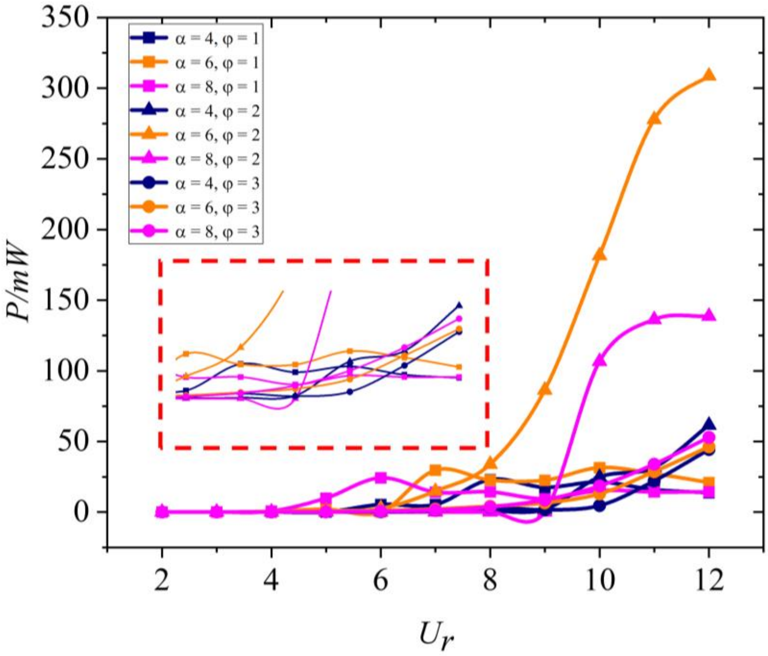

Fig. 19. Diagrammatic of power variation with respect to the reduced velocity of two square cross-section cylinders in tandem.

5. Conclusions

This paper mainly conducts a numerical analysis on the series circular cylinders and series square cylinders. The paper presents a detailed study on the influence of different spacing ratios α and different radius ratios φ on the series two-cylinder system. The conclusions are as follows:

(1) As the spacing ratio α increases, the series circular-cylinder system exhibits classic vortex-induced vibration. When $\varphi = 2$, the vibration of the downstream cylinder still shows irregular VIV, and the lock-in interval is not observed. When $\varphi = 3$, the dimensionless amplitude curve of the downstream vibrating cylinder has obvious fluctuations, but it cannot be seen whether it is VIV or galloping in this case.

(2) The series square-cylinder system has a sudden drop at $\varphi = 1$, $\alpha = 5.5$ and $6 \leq U_r \leq 8$. Subsequently, the cases of $\alpha = 5.3$ - 5.7 are further analyzed. It can be found that when $\alpha = 5.6$, the sudden drop interval is advanced. When $\alpha = 5.7$, there is a hysteresis in the sudden drop interval, and the corresponding dimensionless frequency does not appear sudden drop or lock-in. Therefore, for the series square-cylinder system, the vibration of the downstream cylinder can be effectively suppressed when $\alpha = 5.3$ - 5.7, $6 \leq U_r \leq 8$. Due to space limitations, in future work, a detailed analysis of the vortex in the suppressed state can be performed to judge the change of the wake vortex in the suppressed region.

(3) When changing the radius ratio of the square cylinders arranged in series, it is found that as the radius ratio increases, the vibration of the downstream vibrating cylinder transitions from VIV to galloping. When $\varphi = 1$, the dimensionless amplitudes of the three spacing ratio cases all reflect the characteristics of VIV and the cases show galloping when $\varphi = 2$ and 3. When $\varphi = 2$, $\alpha = 4$ and 8, the dimensionless amplitude of the downstream cylinder is close to 0 in the interval of $2 \leq U_r \leq 9$ and then increases

in the interval of $9 \leq U_r \leq 12$. However, the dimensionless amplitude becomes larger as the reduced velocity increases when $\alpha = 6$.

(4) Having analysed the energy harvesting power, it can be stated that the highest power is achieved at $\varphi = 2$ and $\alpha = 6$, whereas at $\varphi = 2$ and $\alpha = 6$ it has the second highest peak. While in other cases the power is just between 0 - 50mW.

(5) Short-time Fourier transform and Morlet wavelet transform are used to perform time-frequency analysis on different cases of changing the radius ratio. It can be found that the frequency characteristics of the series square-cylinder system are more complicated than that of the series circular-cylinder system and show more frequency components. This also explains the phenomenon that galloping occurs in the series square-cylinder system with the increase of radius ratio, while the circular-cylinder system only maintains the VIV or irregular VIV.

Acknowledgments

This project was supported by National Natural Science Foundation of China (Grant No. 52165010, Liuzhou Science and Technology Plan Project: Research and Application of Key Technologies for Active and Passive Composite Control of Low-Frequency Noise of Commercial Vehicles (2020PAA0604), Liuzhou Science and Technology Plan Project: Development of key technologies for improving the fuel economy of commercial vehicles (2021AAA0108), Natural Science Foundation of Excellent Youth of Henan Province: 222300420076 and National Natural Science Foundation of China (Grant No.: 51977196).

References

[1] Williamson, C.H.K. and R. Govardhan, Vortex-induced vibrations. Annual Review of Fluid Mechanics, 2004. 36: p. 413-455.

[2] Zhu, H.J., T. Tang, Y. Gao, et al., Flow-induced vibration of a trapezoidal cylinder placed at typical flow orientations. Journal of Fluids and Structures, 2021. 103.

[3] Wang, J.L., S.K. Sun, L.H. Tang, et al., On the use of metasurface for Vortex-Induced vibration suppression or energy harvesting. Energy Conversion and Management, 2021. 235.

[4] Bokaian, A. and F. Geoola, Wake-induced galloping of two interfering circular cylinders. Journal of Fluid Mechanics, 2006. 146: p. 383-415.

[5] Assi, G.R.S., P.W. Bearman, N. Kitney, et al., Suppression of wake-induced vibration of tandem cylinders with free-to-rotate control plates. Journal of Fluids and Structures, 2010. 26(7-8): p. 1045-1057.

[6] Assi, G.R.S., P.W. Bearman, and J.R. Meneghini, On the wake-induced vibration of tandem circular cylinders: the vortex interaction excitation mechanism. Journal of Fluid Mechanics, 2010. 661: p. 365-401.

[7] Assi, G.R.S., P.W. Bearman, B.S. Carmo, et al., The role of wake stiffness on the wake-induced vibration of the downstream cylinder of a tandem pair. Journal of Fluid Mechanics, 2013. 718: p. 210-245.

[8] Alam, M.M., Effects of Mass and Damping on Flow-Induced Vibration of a Cylinder Interacting with the Wake of Another Cylinder at High Reduced Velocities. Energies, 2021. 14(16).

[9] Bourguet, R. and D. Lo Jacono, In-line flow-induced vibrations of a rotating cylinder. Journal of Fluid Mechanics, 2015. 781: p. 127-165.

[10] Munir, A., M. Zhao, H.L. Wu, et al., Flow-induced vibration of a rotating circular cylinder at high reduced velocities and high rotation rates. Ocean Engineering, 2021. 238.

[11] Song, H., W.P. Huang, X.P. Fu, et al., Empirical model of the wake-induced lift force on a cylinder with low mass ratio. Marine Structures, 2021. 80.

[12] Chaplin, J.R. and W.M.J. Batten, Simultaneous Wake- and Vortex-Induced Vibrations of a Cylinder With Two Degrees of Freedom in Each Direction. Journal of Offshore Mechanics and Arctic Engineering-Transactions of the Asme, 2014. 136(3).

[13] Tamimi, V., S.T.O. Naeeni, and M. Zeinoddini, Flow induced vibrations of a sharp edge square cylinder in the wake of a circular cylinder. Applied Ocean Research, 2017. 66: p. 117-130.

[14] Zhang, B.S., B.W. Song, Z.Y. Mao, et al., Numerical investigation on VIV energy harvesting of bluff bodies with different cross sections in tandem arrangement. Energy, 2017. 133: p. 723-736.

[15] Bernitsas, M.M., K. Raghavan, Y. Ben-Simon, et al., VIVACE (vortex induced vibration aquatic clean energy): A new concept in generation of clean and renewable energy from fluid flow. Journal of Offshore Mechanics and Arctic Engineering-Transactions of the Asme, 2008. 130(4).

[16] Mehmood, A., A. Abdelkefi, M.R. Hajj, et al., Piezoelectric energy harvesting from vortex-induced vibrations of circular cylinder. Journal of Sound and Vibration, 2013. 332(19): p. 4656-4667.

[17] Latif, U., E. Uddin, M.Y. Younis, et al., Experimental electro-hydrodynamic investigation of flag-based energy harvesting in the wake of inverted C-shape cylinder. Energy, 2021. 215.

[18] Ding, L., L. Zhang, M.M. Bernitsas, et al., Numerical simulation and experimental validation for energy harvesting of single-cylinder VIVACE converter with passive turbulence control. Renewable Energy, 2016. 85: p. 1246-1259.

[19] Zhang, C.Y., G. Hu, D. Yurchenko, et al., Machine learning based prediction of piezoelectric energy harvesting from wake galloping. Mechanical Systems and Signal Processing, 2021. 160.

[20] Ding, L., L. Zhang, C.M. Wu, et al., Flow induced motion and energy harvesting of bluff bodies with different cross sections. Energy Conversion and Management, 2015. 91: p. 416-426.

[21] Wang, J.L., Z. Su, H. Li, et al., Imposing a wake effect to improve clean marine energy harvesting by flow-induced vibrations. Ocean Engineering, 2020. 208: p. 107455.

[22] Menter, F.R., 2-EQUATION EDDY-VISCOSITY TURBULENCE MODELS FOR ENGINEERING APPLICATIONS. Aiaa Journal, 1994. 32(8): p. 1598-1605.

[23] Zhang, B.S., Z.Y. Mao, B.W. Song, et al., Numerical investigation on effect of damping-ratio and mass-ratio on energy harnessing of a square cylinder in FIM. Energy, 2018. 144: p. 218-231.

[24] Zhang, B.S., K.H. Wang, B.W. Song, et al., Numerical investigation on the effect of the cross-sectional aspect ratio of a rectangular cylinder in FIM on hydrokinetic energy conversion. Energy, 2018. 165: p. 949-964.

[25] Huera-Huarte, F.J. and M. Gharib, Vortex- and wake-induced vibrations of a tandem arrangement of two flexible circular cylinders with far wake interference. Journal of Fluids and Structures, 2011. 27(5-6): p. 824-828.

[26] Nguyen, V.T., W.H.R. Chan, and H.H. Nguyen, Numerical investigation of wake induced vibrations of cylinders in tandem arrangement at subcritical Reynolds numbers. Ocean Engineering, 2018. 154: p. 341-356.

[27] Lin, K., D.X. Fan, and J.S. Wang, Dynamic response and hydrodynamic coefficients of a cylinder oscillating in crossflow with an upstream wake interference. Ocean Engineering, 2020. 209.

[28] Zhu, H.J., Y. Zhao, and T.M. Zhou, CFD analysis of energy harvesting from flow induced vibration of a circular cylinder with an attached free-to-rotate pentagram impeller. Applied Energy, 2018. 212: p. 304-321.

[29] Ohashi, K., A new approach for handling body motion by combining a grid deformation method and an overset grids technique. Ocean Engineering, 2020. 213: p. 107836.

[30] Zhu, H.J., C. Zhang, and W.L. Liu, Wake-induced vibration of a circular cylinder at a low Reynolds number of 100. Physics of Fluids, 2019. 31(7).

[31] Bernitsas, M.M., J. Ofuegbe, J.U. Chen, et al. EIGEN-SOLUTION FOR FLOW INDUCED OSCILLATIONS (VIV & GALLOPING) REVEALED AT THE FLUID -STRUCTURE INTERFACE. in 38th ASME International Conference on Ocean, Offshore and Arctic Engineering (OMAE 2019). 2019. Univ Strathclyde, Glasgow, SCOTLAND.

[32] Farge, M., WAVELET TRANSFORMS AND THEIR APPLICATIONS TO TURBULENCE. Annual Review of Fluid Mechanics, 1992. 24: p. 395-457.

[33] Leao, R.N. and J.A. Burne, Continuous wavelet transform in the evaluation of stretch reflex responses from surface EMG. Journal of Neuroscience Methods, 2004. 133(1-2): p. 115-125.

[34] Chen, W.L., C.N. Ji, R. Wang, et al., Flow-induced vibrations of two side-by-side circular cylinders: Asymmetric vibration, symmetry hysteresis and near-wake patterns. Ocean Engineering, 2015. 110: p. 244-257.

[35] Zhao, M., L. Cheng, and H.W. An, Numerical investigation of vortex-induced vibration of a circular cylinder in transverse direction in oscillatory flow. Ocean Engineering, 2012. 41: p. 39-52.

[36] Wang, J.L., Z. Su, H. Li, et al., Imposing a wake effect to improve clean marine energy harvesting by flow-induced vibrations. OCEAN ENG, 2020. 208: p. 107455.